

# Insights into the Storage Mechanism of Layered VS<sub>2</sub> Cathode in Alkali Metal-Ion Batteries

Xiao Zhang, Qiu He, Xiaoming Xu, Tengfei Xiong, Zhitong Xiao, Jiashen Meng, Xuanpeng Wang, Lu Wu, Jinghui Chen, and Liqiang Mai\*

VS<sub>2</sub> is one of the attractive layered cathodes for alkali metal-ion batteries. However, the understanding of the detailed reaction processes and energy storage mechanism is still inadequate. Herein, the Li<sup>+</sup>/Na<sup>+</sup>/K<sup>+</sup> insertion/extraction mechanisms of VS<sub>2</sub> cathode are elucidated on the basis of experimental analyses and theoretical simulations. It is found that the insertion/extraction behavior of Li<sup>+</sup> is partially irreversible, while the insertion/extraction behavior of Na<sup>+</sup>/K<sup>+</sup> is completely reversible. The detailed intermediates and final products (Li<sub>0.33</sub>VS<sub>2</sub>, LiVS<sub>2</sub>, Na<sub>0.5</sub>VS<sub>2</sub>, NaVS<sub>2</sub>, K<sub>0.6</sub>VS<sub>2</sub>, K<sub>z</sub>VS<sub>2</sub>, z > 0.6) during the discharging/charging processes are identified, indicating that VS<sub>2</sub> undergoes different phase transitions and solid–solution reactions in different battery systems, which have a great influence on the battery performance. Moreover, the diffusion of Na<sup>+</sup> in VS<sub>2</sub> cathode is demonstrated to be much slower than that of Li<sup>+</sup> and K<sup>+</sup>. Such mechanistic research provides a reference for in-depth understanding of energy storage in layered transition metal sulfides/selenides.

great attention as alternatives to LIBs, in order to provide new opportunities for the substantial improvement of energy storage systems.<sup>[5–12]</sup> The alkali metals (Li, Na, and K) are located at the first group in the periodic table, possessing similar physicochemical properties. However, it is generally accepted that the larger cation radius of Na<sup>+</sup> (1.02 Å) and K<sup>+</sup> (1.33 Å) causes the sluggish diffusion kinetics, thus limiting the development of SIBs and PIBs.<sup>[6]</sup> Compared to the mature technology of LIBs, the developments of SIBs and PIBs are still at an initial stage.

The common electrode materials in LIBs are generally not applicable to SIBs and PIBs.<sup>[13–18]</sup> Advanced electrode materials that can store large-sized Na<sup>+</sup> and K<sup>+</sup> are urgently desired. 2D layered transition metal dichalcogenides (TMDs), which are fundamentally and technically interesting,

have been widely researched in energy storage field.<sup>[19–21]</sup> Vanadium disulfide (VS<sub>2</sub>) is a typical family member of TMDs, which has attracted wide attention due to its layered structure with a large interlayer spacing of 0.57 nm together with excellent electric conductivity and weak van der Waals interlayer interaction.<sup>[22,23]</sup> The unique structure and properties of VS<sub>2</sub> make it an ideal host for the insertion/extraction of alkali metal-ions. Recently, the literature regarding the potential of VS<sub>2</sub> as an electrode for alkali metal-ion (Li<sup>+</sup>, Na<sup>+</sup>, and K<sup>+</sup>) batteries with outstanding performance has been reported.<sup>[24–29]</sup> However, less attention has been paid to the relationship between the electrochemical performance and the storage mechanism in alkali metal-ion batteries. Revealing the detailed energy storage mechanisms, including the structural evolution, phase transition reactions, and ion diffusion kinetics, is highly significant for a deeper understanding of the electrochemistry about VS<sub>2</sub> and further optimization of its electrochemical performance in alkali metal-ion batteries.

In this work, we systematically revealed and compared the electrochemical behaviors of the layered VS<sub>2</sub> cathode in three battery systems (LIBs, SIBs, and PIBs), including electrochemical performance, detailed structural evolution, and reaction kinetics during the alkali metal-ions insertion/extraction. In situ X-ray diffraction (XRD), ex situ transmission electron microscope (TEM), together with density functional theory (DFT) analysis were employed to accurately track the structural evolution of VS<sub>2</sub> during the discharging/charging processes,

## 1. Introduction


Lithium ion batteries (LIBs) have been widely applied to consumer electronic products due to its high voltage, high energy density, and environment-friendly characteristics since its commercialization in 1991.<sup>[1–4]</sup> With the advent of large-scale energy storage systems, sodium ion batteries (SIBs) and potassium ion batteries (PIBs) have recently attracted

X. Zhang, Q. He, Dr. X. Xu, Z. Xiao, J. Meng, L. Wu, J. Chen, Prof. L. Mai  
State Key Laboratory of Advanced Technology for Materials Synthesis  
and Processing

School of Materials Science and Engineering  
Wuhan University of Technology  
Wuhan 430070, P. R. China  
E-mail: mlq518@whut.edu.cn

T. Xiong  
Department of Chemistry  
City University of Hong Kong  
Kowloon, Hong Kong SAR 999077, P. R. China

Dr. X. Wang  
Department of Physical Science & Technology  
School of Science  
Wuhan University of Technology  
Wuhan 430070, P. R. China

 The ORCID identification number(s) for the author(s) of this article can be found under <https://doi.org/10.1002/aenm.201904118>.

DOI: 10.1002/aenm.201904118

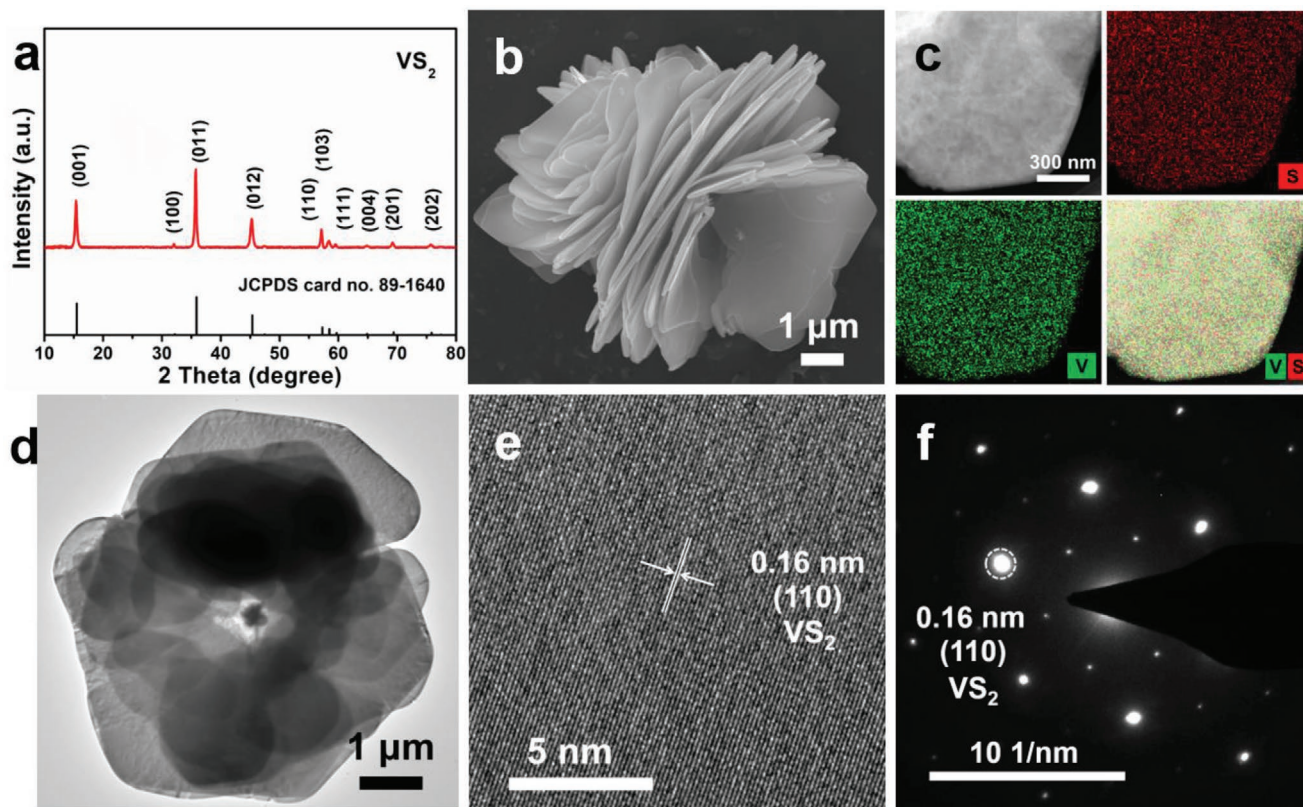


**Figure 1.** XRD pattern (a), SEM image (b), EDX mappings (c), TEM image (d), HRTEM image (e), and SAED pattern (f) of  $\text{VS}_2$  nanosheets.

which gives a clear understanding of the characteristics of phase transition or solid–solution reactions at each stage.

## 2. Results and Discussion

The XRD pattern of  $\text{VS}_2$  powder identifies the high phase purity (Figure 1a). The diffraction peaks are indexed to the layered hexagonal  $\text{VS}_2$  (JCPDS: 01-089-1640, Table S1, Supporting Information). Figure 1b shows the scanning electron microscope (SEM) image of  $\text{VS}_2$ . The 3D flower structure with a diameter of 3–5  $\mu\text{m}$  is composed of 2D 50–80 nm thickness nanosheets. The energy dispersive X-ray spectrometry (EDX) mappings of the nanosheets reveal a uniform distribution of V and S elements (Figure 1c). Figure 1d demonstrates the 2D structure of  $\text{VS}_2$  nanosheets. Moreover, the high-resolution TEM (HRTEM) image displays clear lattice fringes with a spacing of 0.16 nm, which is indexed to the (110) planes of  $\text{VS}_2$  (Figure 1e). In addition, the selected area electron diffraction (SAED) pattern shows the diffraction spots of  $\text{VS}_2$  (110) planes, indicating the single-crystalline nature of the sample (Figure 1f).

The electrochemical properties of  $\text{Li}/\text{VS}_2$ ,  $\text{Na}/\text{VS}_2$ , and  $\text{K}/\text{VS}_2$  cells (operated within the voltage windows of 1.5–3.5, 1.5–2.8, and 1.5–3.5 V, respectively) were first investigated by cyclic voltammetry (CV) at a scan rate of 0.2  $\text{mV s}^{-1}$  and galvanostatic discharge/charge measurements at a current density of 100  $\text{mA g}^{-1}$ . From the CV curves in LIBs system, two cathodic peaks located at 2.42 and 2.21 V in the initial cycle can be ascribed to the phase

reaction from  $\text{VS}_2$  to  $\text{Li}_x\text{VS}_2$  during  $\text{Li}^+$  insertion. The anodic peaks located at 2.28, 2.36, 2.42, and 2.49 V are observed, which are attributed to  $\text{Li}^+$  extraction from  $\text{Li}_x\text{VS}_2$  (Figure 2a).<sup>[23,25,30,31]</sup> In SIBs system, four oxidation peaks can be noticed in the first cycle at around 2.02, 2.08, 2.25, and 2.35 V, which represent Na-extraction from the  $\text{VS}_2$  host, while only two broad peaks are located at 1.96 and 1.56 V during the reduction process, corresponding to  $\text{Na}^+$  insertion into the  $\text{VS}_2$  cathode (Figure 2b).<sup>[26,32,33]</sup> In PIBs system, three cathodic peaks attributed to  $\text{K}^+$  insertion are located at 2.20, 2.11, and 1.73 V, while three anodic peaks assigned to  $\text{K}^+$  extraction are situated at 1.94, 2.32, and 2.91 V in the initial cycle (Figure 2c).<sup>[34]</sup> The discharge/charge curves of the  $\text{VS}_2$  cathode consist of two discharge plateaus at 2.31 and 2.20 V, and four charge plateaus at around 2.23, 2.32, 2.41, and 2.48 V in LIBs (Figure 2d); two pairs of redox voltage plateaus at 2.11/1.63 and 2.30/1.90 V in SIBs (Figure 2e); two discharge voltage plateaus located at around 2.21 and 1.78 V and four charge voltage plateaus located at about 1.91, 2.47, 2.90, and 3.29 V in PIBs (Figure 2f). It is observed that the reduction and oxidation peaks in three battery systems shift after the first cycle. This phenomenon can be ascribed to the activation of electrode materials in the first cycle.<sup>[26,35]</sup> Furthermore, these different CV curves indicate different reaction mechanisms of  $\text{VS}_2$  nanosheets in three battery systems, and the multiple redox peaks reveal complex evolution processes during the metal-ion insertion/extraction. The cycling performances of the  $\text{VS}_2$  nanosheets in LIBs, SIBs, and PIBs were further tested by galvanostatic discharge/charge cycles at 100  $\text{mA g}^{-1}$  (Figure 2g). The pristine  $\text{VS}_2$

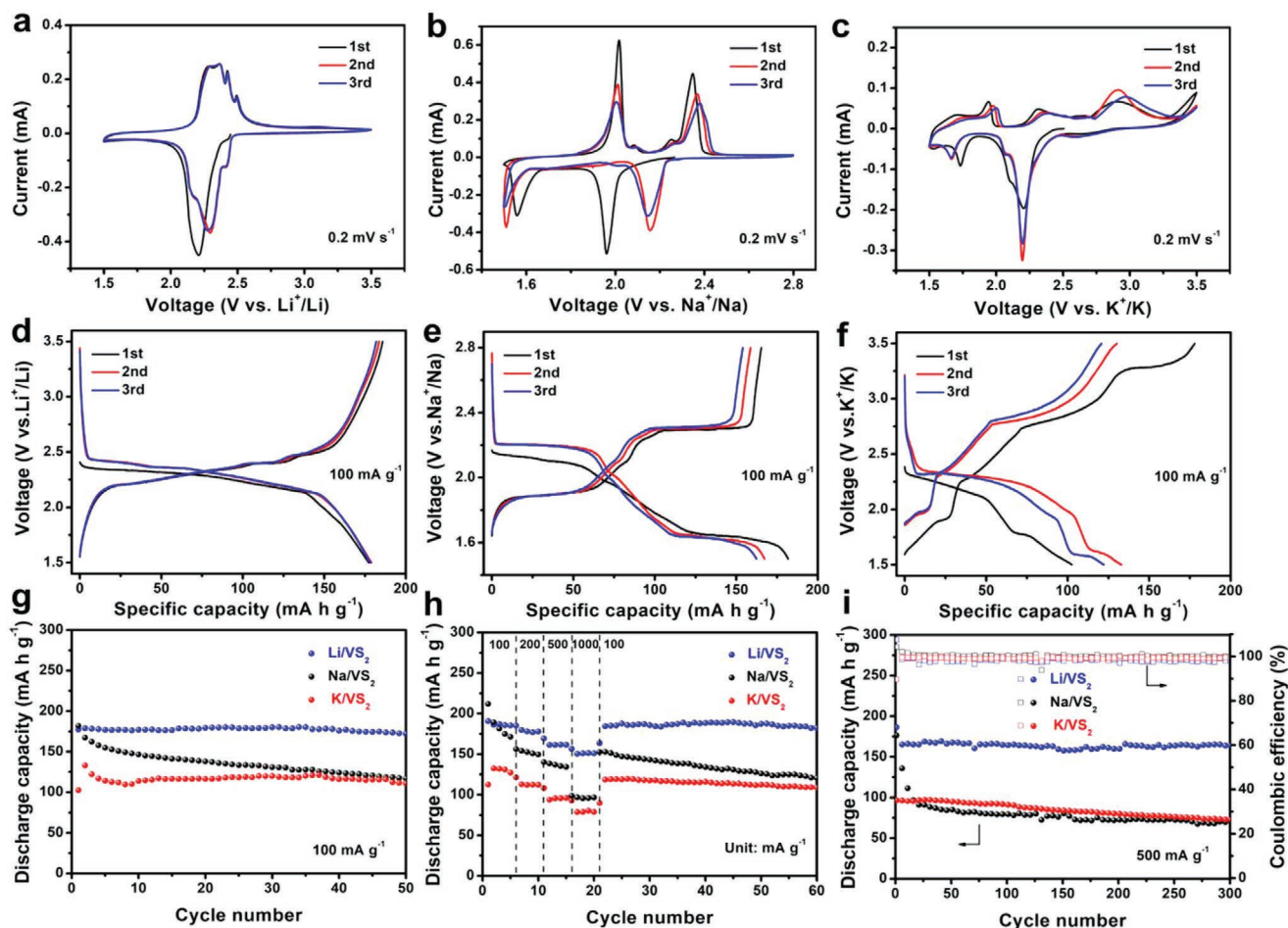


**Figure 2.** CV curves of  $\text{VS}_2$  nanosheets in LIBs (a), SIBs (b), and PIBs (c) at  $0.2 \text{ mV s}^{-1}$ , and discharge/charge profiles of  $\text{VS}_2$  nanosheets in LIBs (d), SIBs (e), and PIBs (f) at  $100 \text{ mA g}^{-1}$ , respectively. Cycling performance at  $100 \text{ mA g}^{-1}$  (g), rate capability at different current rates within  $100\text{--}1000 \text{ mA g}^{-1}$  (h), and long-term cycling performance at  $500 \text{ mA g}^{-1}$  (i) of  $\text{VS}_2$  nanosheets in LIBs, SIBs, and PIBs, respectively.

nanosheets demonstrate discharge capacities of  $172.1$ ,  $116.9$ , and  $111.0 \text{ mA h g}^{-1}$  after 50 cycles in LIBs, SIBs, and PIBs, respectively. The capacity retentions are 97.0% in LIBs, 64.3% in SIBs, and 108.3% in PIBs. The low capacity retention of SIBs indicates that the layered structure of  $\text{VS}_2$  may collapse during  $\text{Na}^+$  insertion/extraction. The coulombic efficiencies of three battery systems are relatively consistent at approximately 100% (excluding the first cycle) (Figure S1a, Supporting Information). The energy efficiencies of both LIBs and SIBs exceed 90%, while that of PIBs are about 75% (excluding the first cycle) due to the large overpotential (Figure S1b, Supporting Information). Such high energy efficiency endows this material with potential application not only in LIBs but also in SIBs and PIBs.<sup>[36]</sup> In addition, the rate capabilities of  $\text{VS}_2$  nanosheets were tested at various current densities (Figure 2h). When tested at  $1000 \text{ mA g}^{-1}$ , the capacity retentions (compared to the capacities at  $100 \text{ mA g}^{-1}$ ) of  $\text{VS}_2$  nanosheets in LIBs, SIBs, and PIBs are 81.3%, 52.1%, and 64.6%, respectively. The long-term cyclic stability of  $\text{VS}_2$  nanosheets in LIBs, SIBs, and PIBs was evaluated at  $500 \text{ mA g}^{-1}$  for 300 cycles (Figure 2i). Interestingly, the  $\text{VS}_2$  nanosheets show a lower specific discharge capacity of  $71.6 \text{ mA h g}^{-1}$  in SIBs and a lower capacity retention of 43.0% than those in LIBs ( $164.8 \text{ mA h g}^{-1}$ , 97.2%)

and PIBs ( $72.8 \text{ mA h g}^{-1}$ , 71.1%) after 300 cycles. In comparison,  $\text{VS}_2$  nanosheets in SIBs exhibit the worst rate performance and cycling stability. The galvanostatic intermittent titration technique (GITT) test results show that the theoretical discharge capacities of  $\text{VS}_2$  nanosheets are  $234.2 \text{ mA h g}^{-1}$  in LIBs,  $238.4 \text{ mA h g}^{-1}$  in SIBs, and  $139.2 \text{ mA h g}^{-1}$  in PIBs, corresponding to the insertion of  $\approx 1.01$  Li-ions,  $\approx 1.02$  Na-ions, and  $\approx 0.60$  K-ion per formula, respectively (Figure S2, Supporting Information).

To elucidate the difference of electrochemical performances in three battery systems, the underlying reaction mechanisms are further explored. In situ XRD measurements were carried out to reveal the phase changes of  $\text{VS}_2$  nanosheets during the first two discharging/charging cycles. The diffraction peak of  $\text{VS}_2$  (001) disappears and the diffraction peak of  $\text{Li}_{0.33}\text{VS}_2$  (001) (JCPDS: 00-034-0751, hexagonal,  $P-3m1$ ; Table S2, Supporting Information) forms during the discharging process in LIBs. Upon further  $\text{Li}^+$  insertion, the  $\text{Li}_{0.33}\text{VS}_2$  structure gradually converts to  $\text{LiVS}_2$  (JCPDS: 01-072-0863; Table S2, Supporting Information), indicating a solid-solution reaction occurs. During the charging process, the  $\text{LiVS}_2$  phase turns into  $\text{Li}_{0.33}\text{VS}_2$ . As de-lithiation continues, the peaks of  $\text{Li}_{0.33}\text{VS}_2$  (JCPDS: 00-034-0820, Monoclinic,  $PE$ ; Table S2,



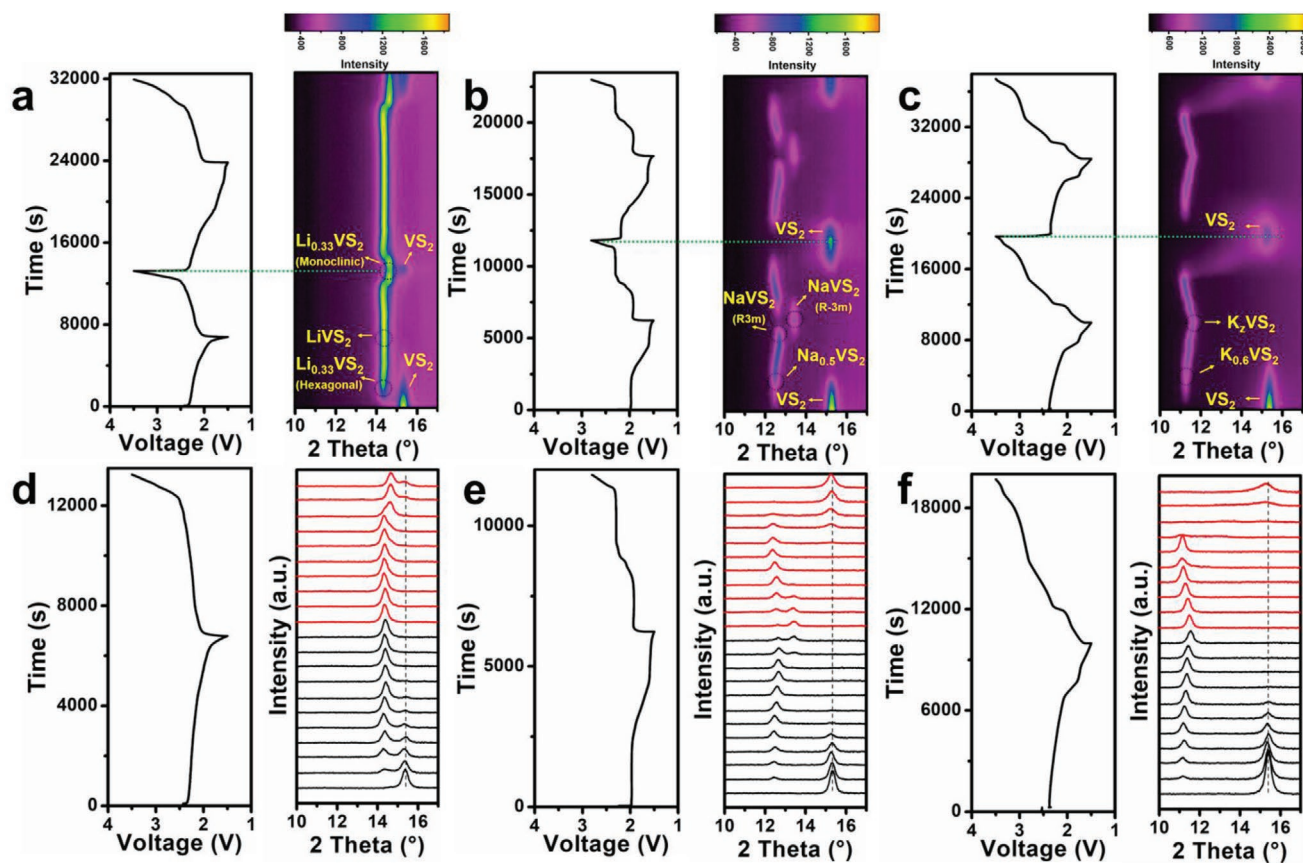


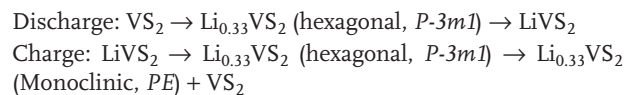
**Figure 3.** 2D in situ XRD patterns during the first two cycles versus galvanostatic discharge/charge times in LIBs (a), SIBs (b), and PIBs (c), respectively. Selected individual diffraction patterns during the first cycle stacked against the voltage profile in LIBs (d), SIBs (e), and PIBs (f), respectively.

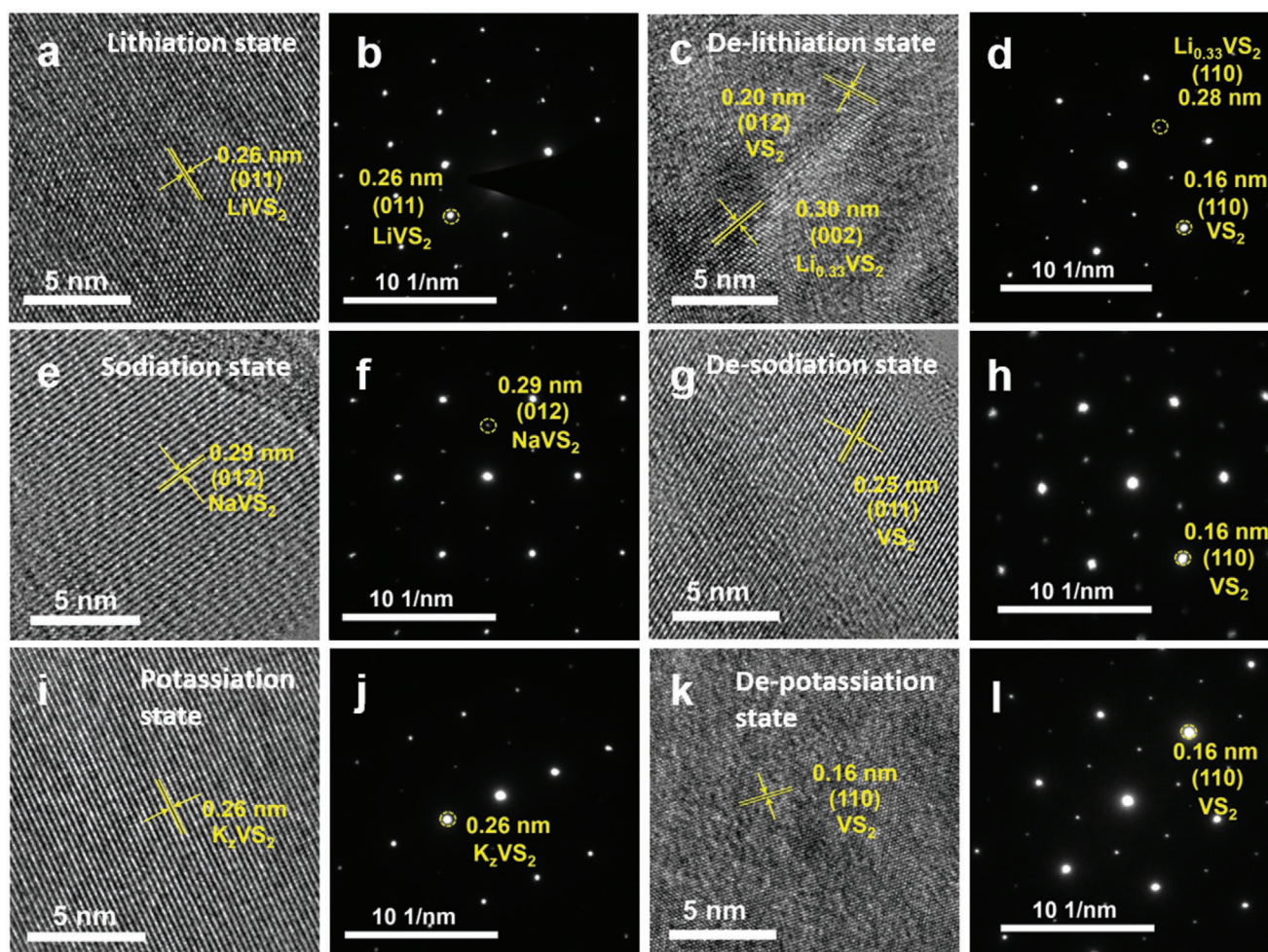
Supporting Information) and  $\text{VS}_2$  are observed, indicating the overall phase transition to  $\text{VS}_2$  is partly irreversible. During the second cycle, the evolution of the reflections is completely reversible, suggesting the different mechanisms between the first and subsequent cycles (Figure 3a,d; Figures S3 and S6a, Supporting Information). The phase transition from  $\text{VS}_2$  to the  $\text{Na}_{0.5}\text{VS}_2$  (JCPDS: 01-089-5280, Table S3, Supporting Information) phase occurs at the beginning of  $\text{Na}^+$  insertion. Along with the further  $\text{Na}^+$  insertion, a solid-solution reaction between  $\text{Na}_{0.5}\text{VS}_2$  and  $\text{NaVS}_2$  (JCPDS: 03-065-3667, rhombohedral,  $R\bar{3}m$ ; Table S3, Supporting Information) can be observed. As the continuous  $\text{Na}^+$  insertion process proceeds to the end, some new diffraction peaks appear, which can be indexed to the  $\text{NaVS}_2$  (JCPDS: 01-089-5279, rhombohedral,  $R\bar{3}m$ ; Table S3, Supporting Information) phase. During the charging process, the evolution is basically inverted compared to that of the discharging process, and finally returns to the pristine  $\text{VS}_2$ , revealing a reversible reaction. The structural evolution of  $\text{VS}_2$  during  $\text{Na}^+$  insertion/extraction in the second cycle is exactly the same as that in the first cycle. However, the peak intensity of  $\text{Na}_{0.5}\text{VS}_2$ ,  $\text{NaVS}_2$  ( $R\bar{3}m$ ), and  $\text{NaVS}_2$  ( $R\bar{3}m$ ) is observed to weaken obviously, indicating the structure degradation after  $\text{Na}^+$  insertion/extraction (Figure 3b,e; Figures S4 and S6b, Supporting Information). Similar to the sodium storage mechanism, the potassium storage mechanism is also completely reversible. Upon  $\text{K}^+$  insertion, a set of new peaks appear, which match the phase of  $\text{K}_{0.6}\text{VS}_2$  (JCPDS: 01-072-1030,

Table S4, Supporting Information). Upon further  $\text{K}^+$  insertion, the peaks shift to higher angles until the phase of  $\text{K}_2\text{VS}_2$  ( $z > 0.6$ ) appears, indicating a solid-solution reaction between  $\text{K}_{0.6}\text{VS}_2$  and  $\text{K}_2\text{VS}_2$  occurs. The position of peaks changes reversely during the charging process. After fully charging, the  $\text{VS}_2$  phase is also observed, suggesting a reversible reaction for the phase transition. There is basically no difference in peak intensity of  $\text{K}_{0.6}\text{VS}_2$  and  $\text{K}_2\text{VS}_2$  between the first and second cycles in PIBs, indicating the good structure stability of  $\text{VS}_2$  for  $\text{K}^+$  storage (Figure 3c,f; Figures S5 and S6c, Supporting Information).

Figure 4 shows the HRTEM images and the SAED patterns of  $\text{VS}_2$  nanosheets at a fully discharged/charged state in LIBs, SIBs, and PIBs. The typical lattice fringes and diffraction spots of several intermediate phases ( $\text{LiVS}_2$ ,  $\text{NaVS}_2$ , and  $\text{K}_2\text{VS}_2$ ) and the corresponding final phases ( $\text{Li}_{0.33}\text{VS}_2$ ,  $\text{VS}_2$ ) are clearly indexed. The defined lattice fringes from the HRTEM images show the good crystallinity, while the diffraction spots from the SAED patterns indicate the single-crystalline nature of the intermediates and final phases.

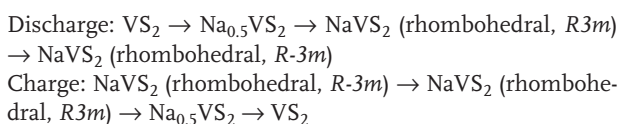
Hence, the phase evolution between  $\text{VS}_2$  and  $\text{Li}_x\text{VS}_2$  during the discharging/charging processes can be proposed as follows:



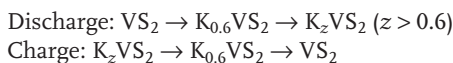


**Figure 4.** HRTEM images and SAED patterns of  $\text{VS}_2$  nanosheets at a,b) lithiation state, c,d) de-lithiation state, e,f) sodiation state, g,h) de-sodiation state, i,j) potassiation state, and k,l) de-potassiation state, respectively.

The phase transition caused by  $\text{Na}^+$  insertion/extraction can be described as follows:



and the overall potassiation/de-potassiation mechanism can be summarized as follows:



To sum up, the structural evolution of  $\text{VS}_2$  in LIBs is partially irreversible: from the initial phase  $\text{VS}_2$  to the  $\text{Li}_{0.33}\text{VS}_2$  (hexagonal,  $P-3m1$ ) phase, and then to the  $\text{LiVS}_2$  phase in  $\text{Li}^+$  insertion process; from the phase of  $\text{LiVS}_2$  to the  $\text{Li}_{0.33}\text{VS}_2$  (hexagonal,  $P-3m1$ ) phase, and then to the mixture phase of  $\text{Li}_{0.33}\text{VS}_2$  (monoclinic,  $PE$ ) and  $\text{VS}_2$  in  $\text{Li}^+$  extraction process. In contrast, the insertion/extraction of  $\text{Na}^+$  and  $\text{K}^+$  is completely reversible.  $\text{VS}_2$  experiences three phases with a completely reversible formation of  $\text{Na}_{0.5}\text{VS}_2$ ,  $\text{NaVS}_2$  (rhombohedral,  $R3m$ ), and

$\text{NaVS}_2$  (rhombohedral,  $R-3m$ ) during  $\text{Na}^+$  insertion/extraction. Meanwhile, the  $\text{K}^+$  insertion/extraction is accompanied by the completely reversible formation of  $\text{K}_{0.6}\text{VS}_2$  and  $\text{K}_z\text{VS}_2$  phases.

Three distinct characteristics are observed from the in situ XRD results. First, during the discharging process of three battery systems, the (001) plane, which is characteristic diffraction of the interlayer spacing, gradually disappears, accompanied by the appearance of new peaks, indicating that a two-phase reaction occurs. As the discharge continues, the position of the peak continuously shifts to a higher angle until the end of the discharge, indicating that a solid-solution reaction occurs. Second, the change of the interlayer spacing directly reflects the crystalline structural change of the material in three battery systems. Based on the Bragg equation, the interlayer spacing of (001) plane in  $\text{VS}_2$  changes from 5.76 to 6.14 Å in LIBs, 5.76 to 7.10 Å in SIBs, and 5.76 to 7.83 Å in PIBs, corresponding to the increment rate of  $\approx 6.69\%$ ,  $\approx 23.42\%$ , and  $\approx 36.11\%$ , respectively (Table S5, Supporting Information). Third, there is one more phase transition process ( $\text{NaVS}_2$ ,  $R3m \rightarrow \text{NaVS}_2$ ,  $R-3m$ ) in SIBs than the other two systems in the structural evolution of the  $\text{VS}_2$ , which may lead to the relatively poor rate and cycling performances in the abovementioned electrochemical tests of SIBs.



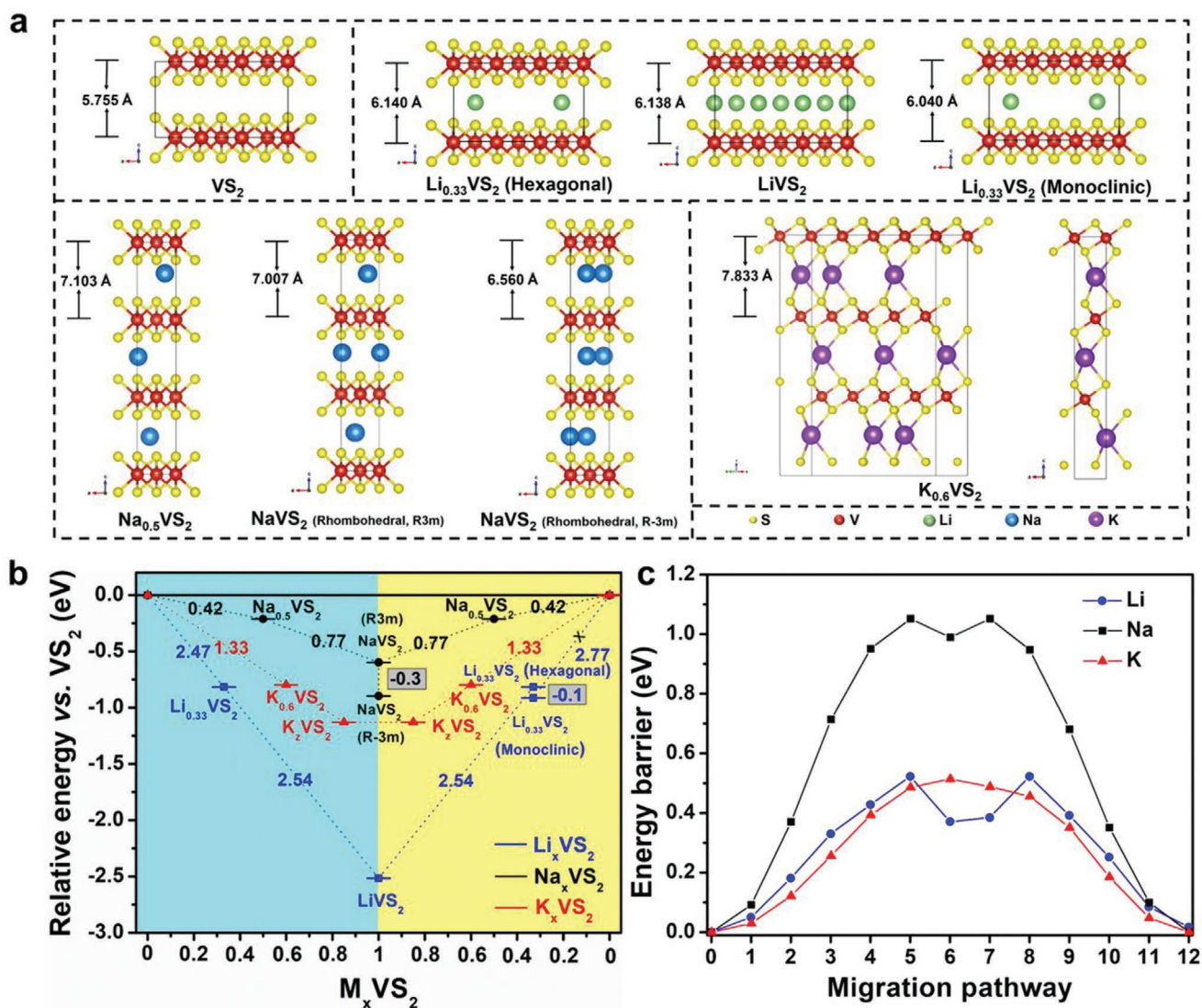


**Figure 5.** a) Crystal structure of  $\text{VS}_2$ ,  $\text{Li}_x\text{VS}_2$ ,  $\text{Na}_x\text{VS}_2$ , and  $\text{K}_{0.6}\text{VS}_2$ . Calculated embedding/disembedding energy (b) and migration energy barriers plots (c) for  $\text{Li}^+$ / $\text{Na}^+$ / $\text{K}^+$  in  $\text{VS}_2$  during the first cycling process.

To confirm this conjecture experimentally, the electrochemical performances of  $\text{VS}_2$  nanosheets in SIBs system were tested in a narrow voltage range (1.8–2.8 V vs  $\text{Na}^+/\text{Na}$ ), and it is found that  $\text{VS}_2$  nanosheets show better electrode stability and longer cycle life than in a wide voltage range (1.5–2.8 V vs  $\text{Na}^+/\text{Na}$ ) (Figure S7, Supporting Information).

The crystal structure of  $\text{VS}_2$ ,  $\text{Li}_x\text{VS}_2$ ,  $\text{Na}_x\text{VS}_2$ , and  $\text{K}_{0.6}\text{VS}_2$  is visually illustrated to show the structural evolution (Figure 5a). Since in situ XRD and ex situ TEM characterizations have confirmed the electrochemical reactions of  $\text{VS}_2$  during the discharging/charging processes, DFT calculations are applied to analyze the energy changes caused by the phase transformations in the first cycle (Figure 5b). During the first discharging process of LIBs,  $\text{VS}_2$  transforms first to  $\text{Li}_{0.33}\text{VS}_2$  and then to  $\text{LiVS}_2$  with the insertion of  $\text{Li}^+$ , which leads to an energy decrease of the system. It is noticed that the insertion energy of per  $\text{Li}^+$  is 2.47 eV in the lithiation of  $\text{VS}_2$  to  $\text{Li}_{0.33}\text{VS}_2$ , and 2.54 eV

per  $\text{Li}^+$  in the further conversion to  $\text{LiVS}_2$ . Subsequently, the  $\text{LiVS}_2$  delithiates to form  $\text{Li}_{0.33}\text{VS}_2$  during the charging process, and the de-lithiation stops for a phase conversion of  $\text{Li}_{0.33}\text{VS}_2$  from hexagonal to monoclinic, which is a more stable phase. The monoclinic  $\text{Li}_{0.33}\text{VS}_2$  will not proceed to delithiate ascribing to the required high de-lithiation energy of 2.77 eV per  $\text{Li}^+$ . For the sodiation of  $\text{VS}_2$ , the  $\text{Na}^+$  insertion energies are 0.42 (from  $\text{VS}_2$  to  $\text{Na}_{0.5}\text{VS}_2$ ) and 0.77 eV (from  $\text{Na}_{0.5}\text{VS}_2$  to  $\text{NaVS}_2$ ), which are lower than  $\text{Li}^+$ . However, there is a space group conversion of rhombohedral  $\text{NaVS}_2$  from  $R3m$  to  $R-3m$  at the end of discharging process, which releases the energy of 0.3 eV per formula of  $\text{NaVS}_2$  ( $R3m$ ). For the potassiation of  $\text{VS}_2$ , the  $\text{K}^+$  gradually intercalates into the interlayer of  $\text{VS}_2$  during the discharging process. The  $\text{K}^+$  insertion energy averages 1.33 eV in the potassiation of  $\text{VS}_2$  to  $\text{K}_{0.6}\text{VS}_2$ . However, the final potassiation state of  $\text{VS}_2$  is uncertain. In short, the insertion of  $\text{Li}^+$  is thermodynamically the easiest, while that of  $\text{Na}^+$  is the

hardest. The calculated insertion and phase transformation energies explain the wholly reversible storage of Na<sup>+</sup>/K<sup>+</sup> and one-third of irreversible lithium storage.

Furthermore, the diffusion kinetics of Li<sup>+</sup>/Na<sup>+</sup>/K<sup>+</sup> in layered VS<sub>2</sub> were simulated by DFT. The migration of Li<sup>+</sup>/Na<sup>+</sup>/K<sup>+</sup> in the layer of VS<sub>2</sub> is along the zigzag pathway, as illustrated in Figure S8a–c, Supporting Information. The transport energy barrier of Na<sup>+</sup> (1.05 eV) is apparently higher than Li<sup>+</sup> and K<sup>+</sup> (0.52 and 0.51 eV), leading to the distinctive worse rate performance in SIBs than that in LIBs and PIBs (Figure 5c). Similar phenomena are also reported in the graphite electrode, but seldom found in layered transition metal sulfides/selenides.<sup>[37,38]</sup>

### 3. Conclusion

In summary, the entire reaction processes and corresponding discharging/charging products of VS<sub>2</sub> nanosheets in the Li<sup>+</sup>/Na<sup>+</sup>/K<sup>+</sup> batteries are systematically investigated by in situ XRD and ex situ TEM, complemented with DFT calculations. VS<sub>2</sub> is found to transform, initially into alkali metal-ions pillared structure, M<sub>x</sub>VS<sub>2</sub> (M = Li, Na, and K; x = 0.33, 0.5 or 0.6), via a two-phase reaction mechanism, followed by the solid-solution reaction to form M<sub>γ</sub>VS<sub>2</sub> (0.33 ≤ γ ≤ 1.0). The structural evolution of VS<sub>2</sub> in LIBs is partially irreversible in the first cycle, while the insertion/extraction of Na<sup>+</sup> and K<sup>+</sup> is completely reversible. A more complex phase transition process and the highest energy barrier for the diffusion of Na<sup>+</sup> cause poor rate performance and more rapid capacity fading in SIBs than the other two systems. Combining electrochemical performance and mechanistic research, our results unravel that VS<sub>2</sub> cathode is more suitable for LIBs and PIBs. This finding provides a new perspective of alkali metal-ions storage mechanisms in VS<sub>2</sub> and also gives enlightening information for the application of other layered transition metal sulfides/selenides in the emerging energy storage systems.

### 4. Experimental Section

**Material Synthesis:** The synthesis of VS<sub>2</sub> nanosheets was modified through a conventional hydrothermal method.<sup>[39]</sup> In a typical synthesis, 2 mL of ammonium hydroxide (NH<sub>3</sub>·H<sub>2</sub>O) was dispersed to 40 mL of deionized water and stirred for 5 min to form a homogeneous solution. Then, 0.234 g of ammonium metavanadate (NH<sub>4</sub>VO<sub>3</sub>) powder was added to this solution and stirred for 10 min to form a uniform, transparent solution. Next, 1.5 g of thioacetamide (C<sub>2</sub>H<sub>5</sub>NS) powder was added and stirred for 1 h at room temperature. Afterward, the above brown dispersion was transferred into Teflon-lined autoclave and maintained at 180 °C for 24 h. Then, the product was collected and washed several times with deionized water and ethanol before being dried at 80 °C in vacuum. Finally, the VS<sub>2</sub> nanosheets were acquired after heat treatment under an argon atmosphere at 300 °C for 2 h.

**Electrochemical Measurements:** Electrochemical measurements were performed with CR2016 coin cells. The working electrode was prepared by pasting a mixture of VS<sub>2</sub> nanosheets (70 wt%), acetylene black (20 wt%), and polyvinylidene fluoride (PVDF) (10 wt%) onto the Al foil and then dried in vacuum at 60 °C for 10 h. Lithium foil, sodium foil, and potassium foil were used as the counter electrodes. A polypropylene film (Celgard-2300), the Whatman glass fiber (GF/A),

and the Whatman glass fiber (GF/D) were used as the separator in LIBs, SIBs, and PIBs, respectively. 1 M LiPF<sub>6</sub> in a mixture of ethylene carbonate (EC), dimethyl carbonate (DMC), and ethylene methyl carbonate (EMC) (1:1:1 by volume); 1 M NaClO<sub>4</sub> in EC/propylene carbonate (PC) (1:1 by volume) with 5% fluoroethylene carbonate (FEC); and 0.8 M KPF<sub>6</sub> in EC/diethyl carbonate (DEC) (1:1 by volume) acted as the electrolyte in LIBs, SIBs, and PIBs, respectively. The galvanostatic discharge/charge and GITT measurements were conducted on Land T2001A battery testing stations within a voltage window of 1.5–3.5, 1.5–2.8, and 1.5–3.5 V in LIBs, SIBs, and PIBs, respectively. The current pulse of 20 mA g<sup>-1</sup> for 10 min and the following relaxation for 40 min were applied in GITT test. Cyclic voltammetry (CV) was measured through an Autolab potentiostat/galvanostat.

**Material Characterizations:** The structural and morphological information was collected from XRD (Bruker D8 Discover X-ray diffractometer with Cu-Kα radiation) (λ = 1.5418 Å), SEM (a JEOL-7100F microscope), TEM, HRTEM, and SAED (a JEOL JEM-2100F STEM/EDS microscope). Samples that were ex situ tested needed to be placed in an argon atmosphere.

**Theoretical Calculations:** The energy changes of VS<sub>2</sub> during the discharging/charging processes were calculated by DFT. The geometric optimization of VS<sub>2</sub> and intermediate/final products (Li<sub>0.33</sub>VS<sub>2</sub>, LiVS<sub>2</sub>, Na<sub>0.5</sub>VS<sub>2</sub>, NaVS<sub>2</sub>, K<sub>0.6</sub>VS<sub>2</sub>) were carried out by the CASTEP module implemented in Accelrys Materials Studio software. The VS<sub>2</sub> and lithiated Li<sub>0.33</sub>VS<sub>2</sub>/LiVS<sub>2</sub> were hexagonal phase, while the sodiated and potassiated products were rhombohedral phase. The popular generalized gradient approximation (GGA) Perdew–Burke–Ernzerhof (PBE) functional was utilized for the relaxation of structures. The plane wave cut-off energy was set as 544.2 eV and the separation of k points was 0.04 Å<sup>-1</sup>. Each calculation was allowed to stop when the energy difference between two ionic steps and the lattice force are less than 1 × 10<sup>-5</sup> eV per atom and 0.03 eV Å<sup>-1</sup>, respectively. The energy threshold of electronic self-convergence was 1 × 10<sup>-6</sup> eV per atom. The transport energy barriers of alkali metal-ions in VS<sub>2</sub> was calculated by Climbing Image Nudged Elastic Band method. The energy difference between two configurations was calculated according to the following equation:

$$E = E(M_{\gamma}VS_2) - E(M_xVS_2) + (x - \gamma)E(M) \quad (1)$$

M refers to alkali metal (M = Li, Na, and K); x and γ refer to stoichiometric numbers of corresponding alkali metal M intercalated in VS<sub>2</sub>. The value of E reflects the alkali metal insertion energy into VS<sub>2</sub> and the thermodynamically required energy for converting M<sub>x</sub>VS<sub>2</sub> to M<sub>γ</sub>VS<sub>2</sub>.

### Supporting Information

Supporting Information is available from the Wiley Online Library or from the author.

### Acknowledgements

X.Z. and Q.H. contributed equally to this work. This work was supported by the National Natural Science Foundation of China (51832004, 51521001, and 21905218), the National Key Research and Development Program of China (2016YFA0202603), the Yellow Crane Talent (Science & Technology) Program of Wuhan City, and the Fundamental Research Funds for the Central Universities (WUT: 203114001).

### Conflict of Interest

The authors declare no conflict of interest.

## Keywords

alkali metal-ion batteries, layered cathodes, reaction mechanisms, VS<sub>2</sub>

Received: December 15, 2019

Revised: March 4, 2020

Published online:

- [1] Z. Yang, J. Zhang, M. C. Kintner-Meyer, X. Lu, D. Choi, J. P. Lemmon, J. Liu, *Chem. Rev.* **2011**, *111*, 3577.
- [2] B. Dunn, H. Kamath, J.-M. Tarascon, *Science* **2011**, *334*, 928.
- [3] M. M. Thackeray, C. Wolverton, E. D. Isaacs, *Energy Environ. Sci.* **2012**, *5*, 7854.
- [4] M. Armand, J. M. Tarascon, *Nature* **2008**, *451*, 652.
- [5] A. Eftekhari, D.-W. Kim, *J. Power Sources* **2018**, *395*, 336.
- [6] J. Liu, *Adv. Funct. Mater.* **2013**, *23*, 924.
- [7] V. Palomares, P. Serras, I. Villaluenga, K. B. Hueso, J. Carretero-González, T. Rojo, *Energy Environ. Sci.* **2012**, *5*, 5884.
- [8] A. Eftekhari, Z. Jian, X. Ji, *ACS Appl. Mater. Interfaces* **2017**, *9*, 4404.
- [9] S. W. Kim, D. H. Seo, X. Ma, G. Ceder, K. Kang, *Adv. Energy Mater.* **2012**, *2*, 710.
- [10] B. Xu, S. Qi, F. Li, X. Peng, J. Cai, J. Liang, J. Ma, *Chin. Chem. Lett.* **2020**, *31*, 217.
- [11] J. C. Pramudita, D. Sehwat, D. Goonetilleke, N. Sharma, *Adv. Energy Mater.* **2017**, *7*, 1602911.
- [12] A. Eftekhari, *ACS Sustainable Chem. Eng.* **2019**, *7*, 5602.
- [13] J. Xu, Y. Dou, Z. Wei, J. Ma, Y. Deng, Y. Li, H. Liu, S. Dou, *Adv. Sci.* **2017**, *4*, 1700146.
- [14] S. Das, D. Swain, R. B. Araujo, S. Shi, R. Ahuja, T. N. G. Row, A. J. Bhattacharyya, *Chem. - Asian J.* **2018**, *13*, 299.
- [15] T. Yang, J. Liang, I. Sultana, M. M. Rahman, M. J. Monteiro, Y. I. Chen, Z. Shao, S. R. P. Silva, J. Liu, *J. Mater. Chem. A* **2018**, *6*, 8280.
- [16] M. Tathavadekar, S. Krishnamurthy, A. Banerjee, S. Nagane, Y. Gawli, A. Suryawanshi, S. Bhat, D. Puthusseri, A. D. Mohite, S. Ogale, *J. Mater. Chem. A* **2017**, *5*, 18634.
- [17] Z. Jian, Z. Xing, C. Bommier, Z. Li, X. Ji, *Adv. Energy Mater.* **2016**, *6*, 1501874.
- [18] M. Shirpour, J. Cabana, M. Doeff, *Energy Environ. Sci.* **2013**, *6*, 2538.
- [19] B. Xu, S. Qi, M. Jin, X. Cai, L. Lai, Z. Sun, X. Han, Z. Lin, H. Shao, P. Peng, *Chin. Chem. Lett.* **2019**, *30*, 2053.
- [20] M. Chhowalla, H. S. Shin, G. Eda, L.-J. Li, K. P. Loh, H. Zhang, *Nat. Chem.* **2013**, *5*, 263.
- [21] J. A. Wilson, A. D. Yoffe, *Adv. Phys.* **1969**, *18*, 193.
- [22] J. Feng, X. Sun, C. Wu, L. Peng, C. Lin, S. Hu, J. Yang, Y. Xie, *J. Am. Chem. Soc.* **2011**, *133*, 17832.
- [23] Y. Jing, Z. Zhou, C. R. Cabrera, Z. Chen, *J. Phys. Chem. C* **2013**, *117*, 25409.
- [24] D. Wu, C. Wang, M. Wu, Y. Chao, P. He, J. Ma, *J. Energy Chem.* **2020**, *43*, 24.
- [25] W. Fang, H. Zhao, Y. Xie, J. Fang, J. Xu, Z. Chen, *ACS Appl. Mater. Interfaces* **2015**, *7*, 13044.
- [26] R. Sun, Q. Wei, J. Sheng, C. Shi, Q. An, S. Liu, L. Mai, *Nano Energy* **2017**, *35*, 396.
- [27] J. Zhou, L. Wang, M. Yang, J. Wu, F. Chen, W. Huang, N. Han, H. Ye, F. Zhao, Y. Li, *Adv. Mater.* **2017**, *29*, 1702061.
- [28] W. Yang, N. Luo, C. Zheng, S. Huang, M. Wei, *Small* **2019**, *15*, 1903904.
- [29] L. Li, Z. Li, A. Yoshimura, C. Sun, T. Wang, Y. Chen, Z. Chen, A. Littlejohn, Y. Xiang, P. Hundekar, *Nat. Commun.* **2019**, *10*, 1.
- [30] D. W. Murphy, J. N. Carides, F. J. Di Salvo, C. Cros, J. V. Waszczak, *Mater. Res. Bull.* **1977**, *12*, 825.
- [31] A. V. Murugan, M. Quintin, M.-H. Delville, G. Campet, K. Vijayamohan, *J. Mater. Chem.* **2005**, *15*, 902.
- [32] D. Wang, Y. Zhao, R. Lian, D. Yang, D. Zhang, X. Meng, Y. Liu, Y. Wei, G. Chen, *J. Mater. Chem. A* **2018**, *6*, 15985.
- [33] D. Zhang, G. Zhao, P. Li, Y. Zhang, W. Qiu, J. Shu, Y. Jiang, S. X. Dou, W. Sun, *Chem. Eur. J.* **2018**, *24*, 1193.
- [34] P. Li, X. Zheng, H. Yu, G. Zhao, J. Shu, X. Xu, W. Sun, S. X. Dou, *Energy Storage Mater.* **2019**, *16*, 512.
- [35] S. Guo, P. Liu, H. Yu, Y. Zhu, M. Chen, M. Ishida, H. Zhou, *Angew. Chem., Int. Ed.* **2015**, *54*, 5894.
- [36] A. Eftekhari, *Sustainable Energy Fuels* **2017**, *1*, 2053.
- [37] Y. Li, Y. Lu, P. Adelhelm, M.-M. Titirici, Y.-S. Hu, *Chem. Soc. Rev.* **2019**, *48*, 4655.
- [38] K. Kubota, M. Dahbi, T. Hosaka, S. Kumakura, S. Komaba, *Chem. Rec.* **2018**, *18*, 459.
- [39] R. Sun, C. Pei, J. Sheng, D. Wang, L. Wu, S. Liu, Q. An, L. Mai, *Energy Storage Mater.* **2018**, *12*, 61.